



# Nonsubsampled shearlet based CT and MR medical image fusion using biologically inspired spiking neural network

Sneha Singh\*, Deep Gupta, R.S. Anand, Vinod Kumar

*Department of Electrical Engineering, Indian Institute of Technology Roorkee, Roorkee 247667, India*



## ARTICLE INFO

### Article history:

Received 2 June 2014

Received in revised form 14 October 2014

Accepted 25 November 2014

Available online 25 March 2015

### Keywords:

Computed tomography (CT)

Image fusion

Magnetic resonance (MR)

Nonsubsampled shearlet transform (NSST)

Pulse coupled neural network

## ABSTRACT

This paper presents a new fusion scheme for the CT and MR medical images that utilizes both the features of the nonsubsampled shearlet transform (NSST) and spiking neural network. As a new image representation with the different features, the NSST is utilized to provide an effective representation of the image coefficients. Firstly, the source CT and MR images are decomposed by the NSST into several subimages. The regional energy is used to fuse the low frequency coefficients. High frequency coefficients are also fused using a pulse coupled neural network model that is used as a biologically inspired type neural network. It also retains the edges and detail information from the source images. Finally, the inverse NSST is used to produce the fused image. The performance of the proposed fusion method is evaluated by conducting several experiments on the different CT and MR medical image datasets. Experimental results demonstrate that the proposed method does not only produce better results by successfully fusing the different CT and MR images, but also ensures an improvement in the various quantitative parameters as compared to other existing methods.

© 2014 Elsevier Ltd. All rights reserved.

## 1. Introduction

Medical images such as MR and CT are very useful in several health care applications such as medical diagnostics, patient health monitoring and drug evaluation. Besides it, various medical imaging modalities become available to support the radiologist representing the information of the different living organs. The magnetic resonance (MR), computed tomography (CT) and ultrasound (US) images are named as structural medical images that provide the structural information of the organs. Others are functional medical images such as functional magnetic resonance (fMR), single photon emission CT (SPECT) that imparts the functional information of the anatomy with lower resolution images. The complete and accurate information is not provided by any one single modality of medical imaging. For example, the MR images reflect the soft tissue information and the CT images present the bony structure information. Therefore, there is a requirement to design an efficient algorithm to integrate both the features in a composite single image. Medical image fusion is a process of merging the

complementary and useful redundant information from the multiple source images obtained from the different imaging modalities into a fused single output image that has special clinical meaning. The fused image is suitable for visual perception, analysis and other computer processing tasks.

In the past few years, various algorithms have been reported in the literature in the field of image fusion. Image fusion can be performed at three different processing levels, viz. pixel, feature and decision level. The pixel level image fusion is further classified as spatial and transform domain [1–3]. The pixel level spatial domain fusion algorithms usually lead to reduce the contrast and also distort the spectral characteristics [4]. Currently, lots of research work on image fusion has been concentrated in the transform domain. In this series, Laplacian pyramid and its different variants have been presented for fusing the multisensor data [5,6]. However, it does not provide any spatial orientation selectivity in the decomposition process, and hence often cause blocking effects/artifacts [7]. Wavelet transform (WT) is one transformation technique that is used for the fusion process [7]. It produces better results and also successfully preserves the spectral information of the input images. In addition to this, the WT is able to capture the one dimensional point singularity [8]. However, it fails to reflect the abrupt transitions such as line and curve singularities. In order to rectify the limitations of the WT, ridgelet transform has been evolved to capture the line singularities of the images

\* Corresponding author at: Department of Electrical Engineering, Indian Institute of Technology Roorkee, Roorkee 247667, Uttarakhand, India. Tel.: +91 9548221323.

E-mail addresses: [singhsneha3026@gmail.com](mailto:singhsneha3026@gmail.com) (S. Singh), [dg268dee@iitr.ac.in](mailto:dg268dee@iitr.ac.in) (D. Gupta), [anandfee@iitr.ac.in](mailto:anandfee@iitr.ac.in) (R.S. Anand), [vinodfee@iitr.ac.in](mailto:vinodfee@iitr.ac.in) (V. Kumar).

[9]. However, it is still unable to represent the curve singularities, effectively. Donoho et al. have used curvelet transform (CVT) to represent two-dimensional singularities of the smooth curve [10]. However, the CVT does not provide a multi-resolution representation of the geometry and also the curvelet cannot be built directly in discrete domain [11]. Further in this series, the contourlet transform improves the fusion results [12,13]. However, Gibbs phenomenon is also present as a result of the lack of shift invariance in contourlet transform [14]. To overcome this problem, the non-subsampled contourlet transform (NSCT) [15] has been introduced and widely used in image fusion schemes. It does not only resolve the problem of capturing the higher dimensional singularity but also inherits a property of shift invariance [14]. However, it has limited number of directions and large computational complexity, whenever it is used in image fusion scheme. To represent more edges, efficiently, Labate et al. introduced a new multiscale geometric analysis tool called shearlet which has all properties like other tools as multiscale, localization, anisotropy and directionality [16], but still it is not able to overcome the problem of shift invariance. Later, Easley et al. [17] proposed nonsubsampled shearlet transform (NSST) that is realized by nonsubsampled Laplacian pyramid (NSLP) and several shearing filters. The NSST provides the variable directional selectivity and shift invariance [14,18,19]. In the recent years, various medical image fusion algorithms based on all these transformation techniques have been reported [11,18,20–27].

Recently developed, pulse coupled neural network (PCNN) which is a biologically inspired spiking neural network [28,29] is efficiently utilized in the different applications of image processing [30]. There are several fusion algorithms that are based on the PCNN and different transformation techniques [24,30–37]. On the basis of results obtained from these algorithms, it is observed that they produce good results, but they have some general problems such as contrast reduction and sometimes the most important fine detail information was lost [35,38,39]. However, in most of the PCNN based image fusion algorithms, the neuron is motivated using one pixel coefficient in spatial domain or in the transform domain. Based on the above concept, the NSST transform and the PCNN model are employed to present the proposed medical image fusion method in which the regional energy is used for fusing low frequency NSST coefficients of the image. The novel sum modified Laplacian (NSML) [40] in the NSST domain is given as an input to motivate the neuron of the PCNN model for high frequency coefficients fusion.

The rest of the paper is organized as follows. Section 2 illustrates the methodologies which are used to present the proposed fusion method. Section 3 presents the implementation of the proposed image fusion method that is based on the NSST. In Section 4, various experimental results are discussed and compared with the existing fusion methods on the basis of different performance measures. Section 5 depicts the final conclusions.

## 2. Methodology

### 2.1. Nonsubsampled shearlet transform

The NSST is an extension of the WT in multidimensional and multidirectional case that combines the multiscale and direction analysis, separately. Firstly, the NSLP is used to decompose an image into low and high-frequency components, and then direction filtering is employed to get the different subbands and different direction shearlet coefficients. The direction filtering is achieved using the shear matrix, which provides various directions. The brief discussion of the NSST is introduced as follows:

Consider a two-dimensional affine system with composite dilations as [17],

$$A_{DS} = \{\psi_{j,k,m}(x) = |\det D|^{j/2} \psi(S^k D^j x - m) : j, k \in \mathbb{Z}, m \in \mathbb{Z}^2\} \quad (1)$$

where  $D$  refers to the anisotropic matrix,  $S$  denotes the shear matrix and  $j, k$  and  $m$  are scale, direction and shift parameter, respectively. The  $D$  and  $S$  are both  $2 \times 2$  invertible matrices and  $|\det S|=1$ . The anisotropic dilation matrix  $\begin{bmatrix} d & 0 \\ 0 & d^{1/2} \end{bmatrix}$  or  $\begin{bmatrix} d^{1/2} & 0 \\ 0 & d \end{bmatrix}$ , where  $d > 0$  controls the scale of shearlets. The shear matrix  $S = \begin{bmatrix} 1 & s \\ 0 & 1 \end{bmatrix}$  or  $\begin{bmatrix} 1 & 0 \\ s & 1 \end{bmatrix}$  controls only the direction of shearlets. The shearlet transform function is

$$\begin{aligned} \psi_{j,k,m}^{(0)}(x) &= 2^{j/2} \psi^{(0)}(S_0^k D_0^j x - m) \text{ and } \psi_{j,k,m}^{(1)}(x) \\ &= 2^{j/2} \psi^{(0)}(S_1^k D_1^j x - m) \end{aligned} \quad (2)$$

where  $j \geq 0, -2^j \leq k \leq 2^j - 1, m \in \mathbb{Z}^2$ ,  $\hat{\psi}^{(0)}(\xi) = \hat{\psi}^{(0)}(\xi_1, \xi_2) = \hat{\psi}_1(\xi_1)\hat{\psi}_2(\xi_2/\xi_1)$  and  $\hat{\psi}^{(1)}(\xi) = \hat{\psi}^{(1)}(\xi_1, \xi_2) = \hat{\psi}_1(\xi_2)\hat{\psi}_2(\xi_1/\xi_2)$ .

As mentioned above, the NSLP and shearing filters (ShF) are utilized to provide the multiscale and multidirectional decomposition. At each NSLP decomposition level, one high frequency and one low frequency sub images are produced and further the low frequency subband is decomposed, iteratively. At the decomposition level  $m=3$ , an image is decomposed into  $m+1=4$  subbands with the same size of the source image in which one subband image is the low frequency component and other  $m$  images are the high frequency subband images. Shearing filter is also used in higher frequency subimages decomposition without sub-sampling which satisfies the shift invariance property. Using the ShF at  $k$  levels, the high frequency subband images obtained from the NSLP at each decomposition level,  $2^k$  directional subband image coefficients are produced with the same size as of the source images. Three level decomposition of the NSST is shown in Fig. 1 which illustrates the NSLP and its corresponding directional decompositions. In this study, the number of shearing directions is taken to be 8, 8 and 4 from finer to coarser scale using three levels NSST decomposition of an image.

### 2.2. Bio-inspired spiking neural network model

Pulse coupled neural network (PCNN) is a biologically inspired feedback neural network [28,29]. The PCNN is a single layer two-dimensional array of laterally linked neurons with one to one correspondence between the image pixels and neurons. In the PCNN model, every pixel is connected to a particular neuron that is also connected to the surrounding neurons in the linking range. Basically, the PCNN neuron consists of three parts such as receptive field, linking modulation field and pulse generator, as shown in Fig. 2. Further, the input signal is divided into linking  $L_{i,j}$  and feeding  $F_{i,j}$  inputs [38,41]. Mathematically, the PCNN model can be given as

$$F_{i,j}[n] = S_{i,j} + e^{-\alpha_F} F_{i,j}[n-1] + V_F \sum_{k,l} M_{i,j,k,l} Y_{i,j}[n-1] \quad (3)$$

$$L_{i,j}[n] = e^{-\alpha_L} L_{i,j}[n-1] + V_L \sum_{k,l} W_{i,j,k,l} Y_{i,j}[n-1] \quad (4)$$

$$U_{i,j}[n] = F_{i,j}[n](1 + \beta L_{i,j}[n]) \quad (5)$$

$$T_{i,j}[n] = e^{-\alpha_T} T_{i,j}[n-1] + V_T Y_{i,j}[n] \quad (6)$$

$$Y_{i,j}[n] = \begin{cases} 1, & U_{i,j} > T_{i,j} \\ 0, & \text{otherwise} \end{cases} \quad (7)$$

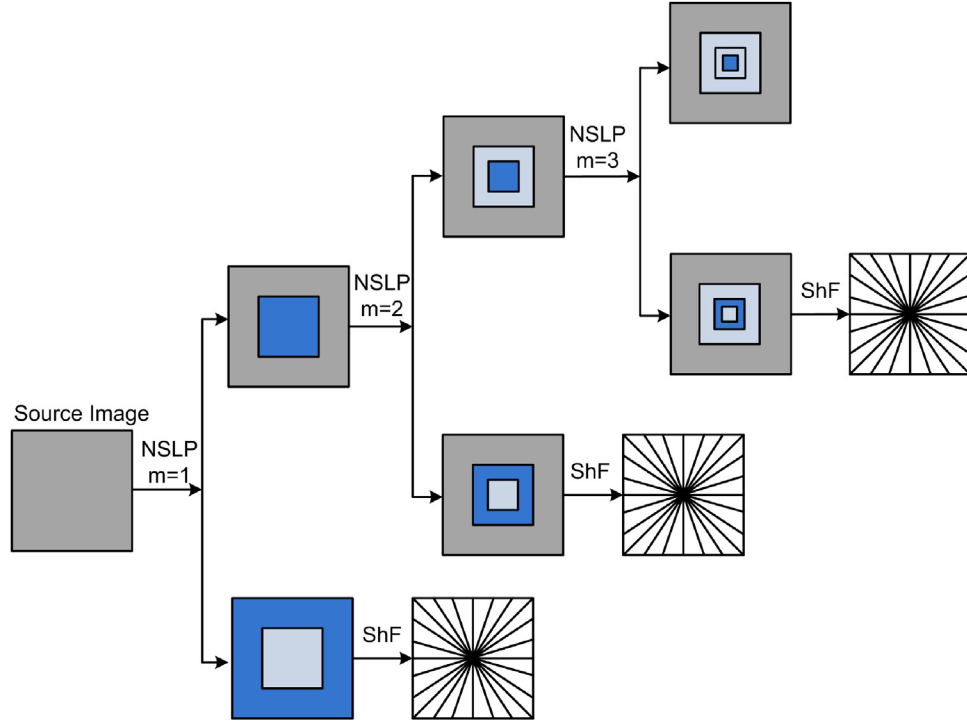


**Fig. 1.** Three level multiscale and multidirectional decomposition of the NSST.

where  $i$  and  $j$  represent the pixel locations,  $k$  and  $l$  refer to the dislocation in a symmetric neighboring pixel,  $n = \{1, 2, 3, \dots, n_{\max}\}$  refers to the current iteration and  $n_{\max}$  is the total number of iterations. The model of PCNN consisting feeding and linking field acquires six parameters such as three decay constants ( $\alpha_F, \alpha_L, \alpha_T$ ) and three normalizing constants ( $V_F, V_L, V_T$ ) for feeding ( $F_{i,j}$ ), linking ( $L_{i,j}$ ) and threshold ( $T_{i,j}$ ) inputs, respectively. In Eqs. (5)–(7),  $U_{i,j}$  is the internal activity of neuron (named as linking modulation) and  $T_{i,j}$  is the dynamic threshold and  $Y_{i,j}$  stands for the pulse output of neurons, respectively. The linking parameter  $\beta$  is an important parameter which varies the weightage of linking field.

### 3. Proposed fusion scheme

For fusing the CT and MR medical images and implementing the above concept, the proposed image fusion method is formulated as follows:

**Step 1:** Start with the given CT and MR images  $X = X_{i,j}$  and  $Y = Y_{i,j}$ , respectively.

**Step 2:** Decompose the original images using the NSST into one low frequency ( $LF$ ) subband and a series of high frequency ( $HF$ ) coefficients at level  $m = 3$  and direction  $k = [2, 3, 3]$  based on repeated experiments from coarser to finer scale of decomposition.

$$[LF_X^{NSST}, HF_X^{NSST}] = NSST(X) \quad \text{and} \quad [LF_Y^{NSST}, HF_Y^{NSST}] = NSST(Y) \quad (8)$$

**Step 3:** For low frequency subband fusion, an activity level measurement such as the regional energy is used because of the LF subband contains most of the signal energy and detail information of the original image. The regional energy is evaluated as

$$G_Z(i, j) = \sum_{i=1}^a \sum_{j=1}^b LF_Z^{NSST}(a+i, b+j)^2 w(i, j) \quad (9)$$

where  $Z$  denotes the original images either  $X$  or  $Y$  and  $w(i, j) = 1/9[1, 1, 1; 1, 1, 1; 1, 1, 1]$  denotes a  $3 \times 3$  template.  $a \times b$  is the size of the template.

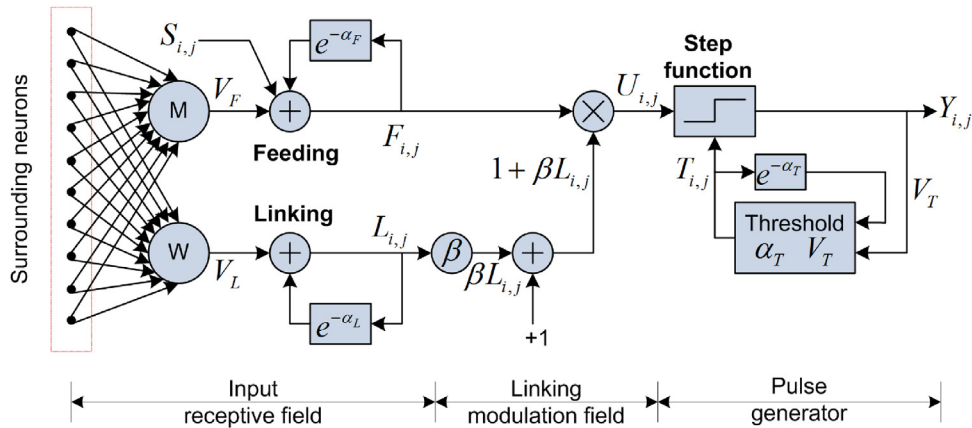


**Fig. 2.** The PCNN model.

**Step 4:** After evaluating the regional energy of both the LF subband of the CT and MR images, a maximum selection rule is applied in choosing the coefficients that have the highest activity measure. It is given as follows:

$$LF_F^{NSST} = \begin{cases} LF_X^{NSST}; & \text{if } |G_X(i,j)| \geq |G_Y(i,j)| \\ LF_Y^{NSST}; & \text{if } |G_X(i,j)| < |G_Y(i,j)| \end{cases} \quad (10)$$

where  $LF_F^{NSST}$  denotes the final fused low frequency subband and F refers to the term fused.

**Step 5:** For the high frequency subbands, compute the NSML as follows:

$$NSML(i,j) = \sum_a \sum_b w(i,j) \cdot F(i+a, j+b) \quad (11)$$

and

$$\begin{aligned} F(i,j) = & |2HF_Z^{NSST}(i,j) - HF_Z^{NSST}(i-1,j) - HF_Z^{NSST}(i+1,j)| \\ & + |2HF_Z^{NSST}(i,j) - HF_Z^{NSST}(i,j-1) - HF_Z^{NSST}(i,j+1)| \end{aligned} \quad (12)$$

where  $w$  is the normalized window and it is defined as,

$$w(i,j) = \begin{bmatrix} 1/15 & 2/15 & 1/15 \\ 2/15 & 3/15 & 2/15 \\ 1/15 & 2/15 & 1/15 \end{bmatrix}$$

**Step 6:** Apply the NSML of each high frequency subband to activate the PCNN and build up the pulse of neurons using the following equations,

$$\left. \begin{aligned} F_{i,j}^Z[n] &= NSML_{i,j}^Z \\ L_{i,j}^Z[n] &= e^{-\alpha L} L_{i,j}^Z[n-1] + V_L \sum_{k,l} W_{i,j,k,l}^Z Y_{i,j}^Z[n-1] \\ U_{i,j}^Z[n] &= F_{i,j}^Z[n](1 + \beta L_{i,j}^Z[n]) \\ T_{i,j}^Z[n] &= e^{-\alpha T} T_{i,j}^Z[n-1] + V_T Y_{i,j}^Z[n] \\ Y_{i,j}^Z[n] &= \begin{cases} 1, & U_{i,j}^Z > T_{i,j}^Z \\ 0, & \text{otherwise} \end{cases} \end{aligned} \right\} \quad (13)$$

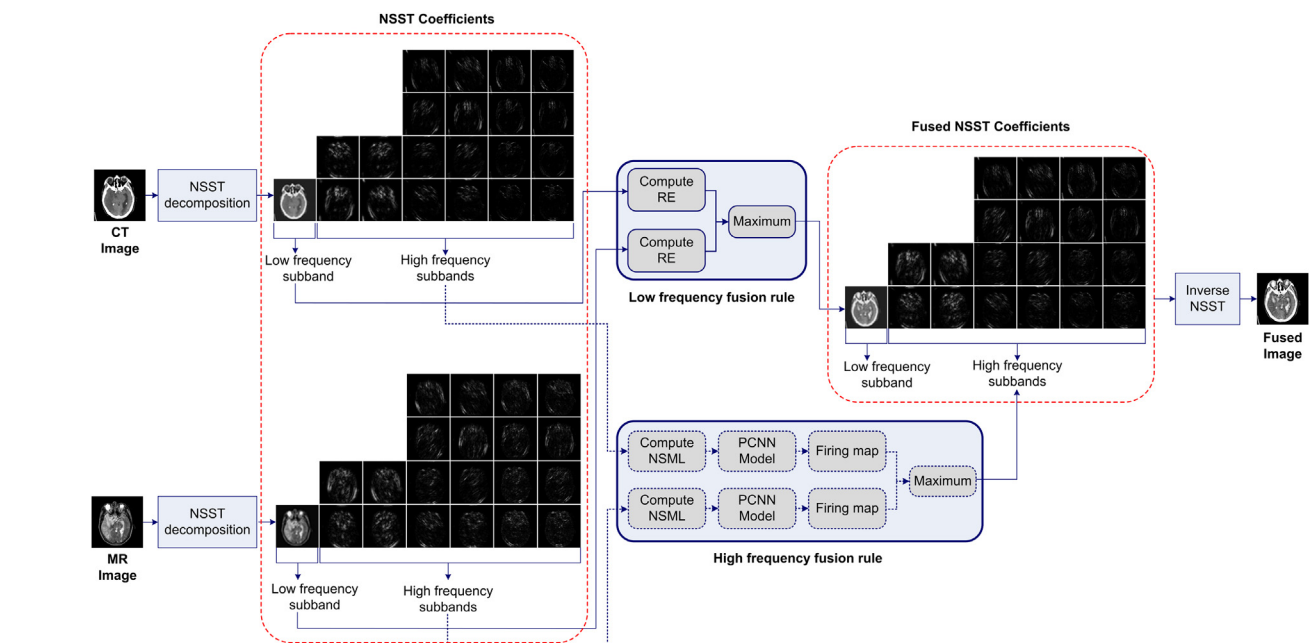


Fig. 3. Process flow of the proposed image fusion method.

**Step 7:** Evaluate the firing times (sum of the  $Y_{i,j}^Z = 1$  or  $U_{i,j}^Z > T_{i,j}^Z$ ) in  $n$  iteration, as follows,

$$t_{i,j}^Z[n] = t_{i,j}^Z[n-1] + t_{i,j}^Z[n] \quad (14)$$

**Step 8:** if  $n = n_{\max}$ , then iteration stops and the high frequency subimage coefficients are fused as the following fusion rule on the basis of the firing time that is evaluated in step 7.

$$HF_F^{NSST} = \begin{cases} HF_X^{NSST}; & \text{if } t_{i,j}^X[n_{\max}] \geq t_{i,j}^Y[n_{\max}] \\ HF_Y^{NSST}; & \text{if } t_{i,j}^X[n_{\max}] < t_{i,j}^Y[n_{\max}] \end{cases} \quad (15)$$

**Step 9:** Perform the inverse NSST ( $NSST^{-1}$ ) on the fused LF and HF subband coefficients to reconstruct the final fused image.

$$F = NSST^{-1}(LF_F^{NSST}, HF_F^{NSST}) \quad (16)$$

The process flow of the proposed CT and MR image fusion method is shown in Fig. 3.

#### 4. Experimentation and analysis of results

A number of illustrative examples are presented to assess the effectiveness of the proposed image fusion method. The fusion results obtained by the proposed method on the different datasets of the CT and MR images are presented. Moreover, the results produced by the proposed method are also compared with the several existing fusion methods in the qualitative and quantitative manner.

##### 4.1. Performance measures

For the quantitative analysis of the performance of the proposed and other methods, commonly used validation parameters such as entropy (EN), standard deviation (STD), spatial frequency (SF), mutual information (MI), image quality index (IQI) and Xydeas and Petrovic metric ( $Q^{XY/F}$ ) have been computed. These measures are defined as follows:

The entropy (EN) is used to measure the information content available in the source image. If the entropy of the fused image gets more than the source images, it denotes the presence of more

information in the fused images. Based on the Shannon information theory, the entropy is defined as,

$$EN = -\sum_{i=0}^{L-1} p(i) \log_2 p(i) \quad (17)$$

where  $p(i)$  is the probability of gray level with a range  $[0, \dots, L-1]$ .

Standard deviation (STD) is used to measure the contrast of individual image. An image  $I(i, j)$  with high contrast will have a high standard deviation. It is defined as,

$$STD = \sqrt{\sum_{i=1}^M \sum_{j=1}^N \frac{[I(i, j) - (1/(M \times N) \sum_{i=1}^M \sum_{j=1}^N I(i, j))]^2}{M \times N}} \quad (18)$$

Spatial frequency (SF) [24,35] is another index that measures the overall activity and clarity level of an image. It is defined as,

$$SF = \sqrt{RF^2 + CF^2} \quad (19)$$

where RF is row frequency and CF is the column frequency and these are evaluated as,

$$RF = \sqrt{\frac{1}{M(N-1)} \sum_{i=1}^M \sum_{j=1}^N (I(i, j-1) - I(i, j))^2} \quad (20)$$

$$CF = \sqrt{\frac{1}{(M-1)N} \sum_{i=2}^M \sum_{j=1}^N (I(i, j) - I(i-1, j))^2} \quad (21)$$

where  $M$  and  $N$  denote the size of the image and  $I(i, j)$  denotes the gray level value of fused image. Higher spatial frequency indicates the better fusion quality.

Mutual information (MI) [24] is used to measure the quality of the fused image. It is defined as

$$MI = I(x_F; x_F) + I(x_Y; x_F) \quad (22)$$

where,  $I(x_R; x_F) = \sum_{u=1}^L \sum_{v=1}^L h_{R,F}(u, v) \log_2 \frac{h_{R,F}(u, v)}{h_R(u)h_F(v)}$  where,  $h_R(u)$ ,  $h_F(v)$  are the normalized gray level histograms of  $x_R$  and  $x_F$ , respectively. The  $h_{R,F}$  is the joint gray level histogram of the  $x_R$  and  $x_F$ . The  $x_R$  and  $x_F$  correspond to the reference and fused image, respectively. If the MI value of fused image is larger, it indicates that the fused image contains more details and texture information.

Image quality index (IQI) [42] between the reference image ( $R$ ) and fused image ( $F$ ) is defined as

$$IQI = \left( \frac{\sigma_{RF}}{\sigma_F \sigma_R} \right) \cdot \left( \frac{2\mu_F \mu_R}{\mu_F^2 + \mu_R^2} \right) \cdot \left( \frac{2\sigma_F \sigma_R}{\sigma_F^2 + \sigma_R^2} \right) \quad (23)$$

where  $\mu_F$ ,  $\mu_R$  are the mean and  $\sigma_F^2$ ,  $\sigma_R^2$  are the variance of the fused and the reference image, respectively. In our study, there are two reference images  $X$  and  $Y$  and one fused image  $I$ . So the quality metric ( $Q_0$ ) is evaluated by averaging  $IQI(X, F)$  and  $IQI(Y, F)$ .

$$IQI = \frac{IQI(X, F) + IQI(Y, F)}{2} \quad (24)$$

If the IQI achieves higher values, i.e. closer to unity, it signifies the better quality of the fused image.

Xydeas and Petrovic [43] presented a performance metric to evaluate the performance of the image fusion methods in terms of edge strength. It is given as

$$Q^{XY/F} = \frac{\sum_{i=1}^M \sum_{j=1}^N Q^{XF}(i, j) w^X(i, j) + Q^{YF}(i, j) w^Y(i, j)}{\sum_{i=1}^M \sum_{j=1}^N w^X(i, j) + w^Y(i, j)} \quad (25)$$

where  $Q^{XF}(i, j) = Q_g^{XF}(i, j) + Q_\alpha^{XF}(i, j)$ . The  $Q_g^{XF}(i, j)$  and  $Q_\alpha^{XF}(i, j)$  here, denote the edge strength and orientation preservation values, respectively. Similarly,  $Q^{YF}(i, j)$  is also evaluated. If the  $Q^{XY/F}$  gets

the value higher and closer to unity, it means that the fused image is produced with less information loss.

## 4.2. Results and discussion

To assess the performance of the proposed fusion approach, different experiments were conducted on two different datasets. First dataset consists of nine different pairs of the CT and MR images (shown in Fig. 4(a) and (b), respectively) taken from Harvard university site (<http://www.med.harvard.edu/AANLIB/home.html>). Second dataset consists of one pair of the CT and MR image (shown in Fig. 5(a) and (b), respectively) acquired from [www.imagefusion.org](http://www.imagefusion.org). All the CT and MR image pairs of the dataset utilized in the present work belong to the same patient. Several experiments are conducted to analyze the performance of the fusion methods on these preregistered CT and MR images. To conduct the experiment, the NSST decomposition level = [2,3,3] and PCNN parameters were set as  $\alpha_L = 0.3$ ,  $\alpha_T = 0.1$ ,  $\beta = 0.2$ ,  $V_L = 1$ ,  $V_T = 10$ ,  $W = \frac{1}{\sqrt{2}} [1 \sqrt{2} 1; \sqrt{2} 0 \sqrt{2}; 1 \sqrt{2} 1]$  and maximum number of iterations  $n_{max} = 200$ . All these parameters are decided based on the repeated experiments. Further, the superiority of the proposed CT and MR image fusion method is assessed by comparing its results with the following existing fusion methods:

**Method 1:** Wavelet based image fusion (WT\_AVG\_MAX) in which the averaging is used for the low frequency approximation fusion and maximum selection rule for the fusion of high frequency detail subimages [7,44].

**Method 2:** Fusion method based on the NSCT decomposition with averaging and maximum (NSCT\_AVG\_MAX) for low and high frequency coefficients, as described in [44] with decomposition level = [4,8,8,16].

**Method 3:** NSST based image fusion method with similar fusion rules as method 2 (NSST\_AVG\_MAX) as shown in [11] with decomposition level = [2,3,3].

**Method 4:** Image fusion method in the NSCT domain using maximum selection and the spatial frequency based PCNN (NSCT\_MAX\_SF\_PCNN) as described in [24,35] with the NSCT decomposition level = [1,2,4] and PCNN parameter  $\alpha_L = 0.06931$ ,  $\alpha_T = 0.2$ ,  $\beta = 0.2$ ,  $V_L = 1$ ,  $V_T = 20$ ,  $n = 200$  and  $W = [0.707, 1, 0.707; 1, 0, 1; 0.707, 1, 0.707]$ . Maximum selection and SF\_PCNN are used for the fusion of low and high frequency subbands, respectively.

**Method 5:** NSCT based CT and MR fusion method using maximum selection rule and the MSF motivated PCNN model (NSCT\_MAX\_MSF\_PCNN) as discussed in [24] with similar parameters as method 4.

**Method 6:** The PCNN based fusion method in the NSST domain with maximum selection rule as described in [37] and named as the NSST\_MAX\_SF\_PCNN. In this method, each PCNN neuron is motivated by the SF of the high frequency subimages of the NSST.

**Method 7:** NSST based image fusion using the similar fusion rule as max selection and MSF motivated PCNN model (NSST\_MAX\_MSF\_PCNN) with the decomposition level = [2,3,3] and the PCNN parameters as  $\alpha_L = 0.3$ ,  $\alpha_T = 0.1$ ,  $\beta = 0.2$ ,  $V_L = 1$ ,  $V_T = 10$ ,

$$W = \frac{1}{\sqrt{2}} \begin{bmatrix} 1 & \sqrt{2} & 1 \\ \sqrt{2} & 0 & \sqrt{2} \\ 1 & \sqrt{2} & 1 \end{bmatrix} \text{ and the maximum number of iterations } = 200.$$

**Method 8:** Image fusion using PCNN model in NSCT domain named as the NSCT.RE.NSML\_PCNN in which regional energy is used for fusing the low frequency subband and the NSML motivated PCNN model is utilized for the fusion of high frequency NSCT coefficients as described in [40] with the similar parameters and decomposition level as method 4.

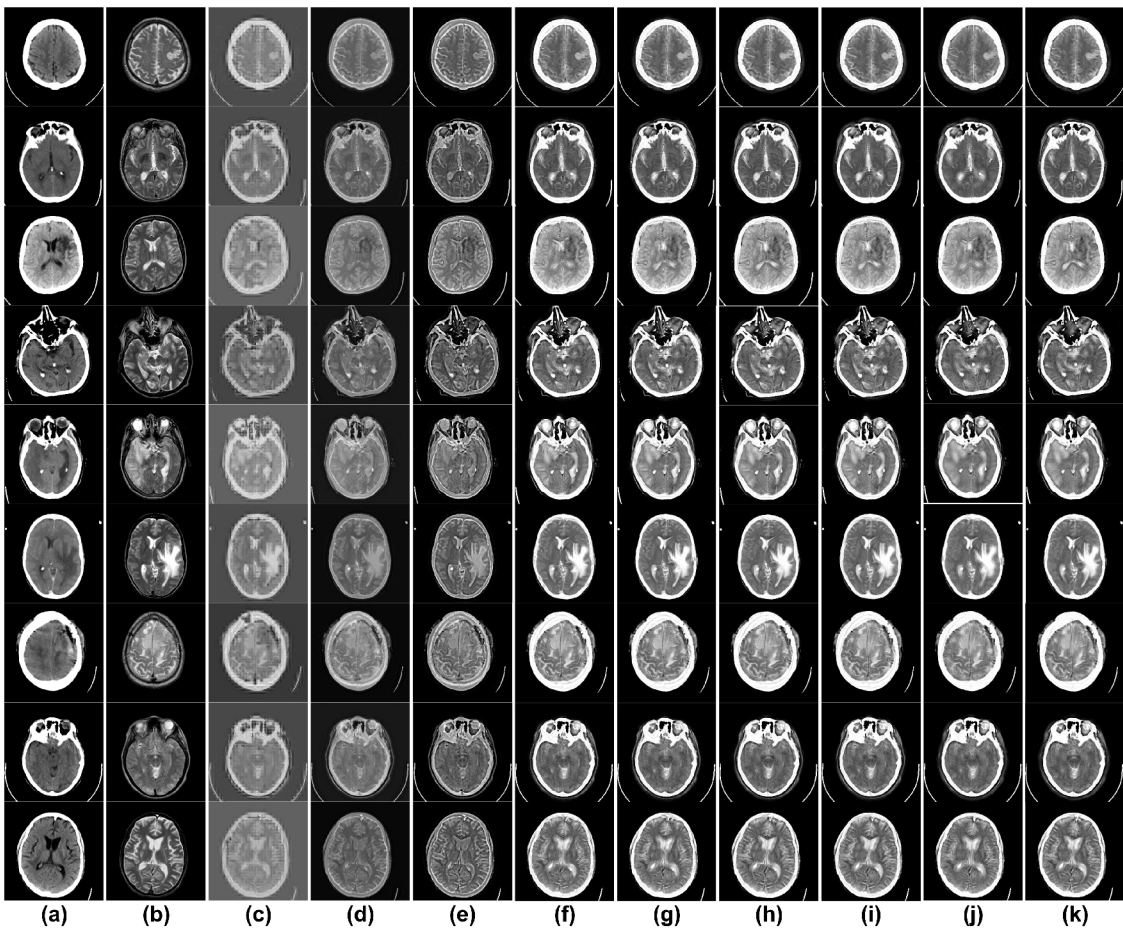


**Fig. 4.** Comparative results of the different fusion methods applied to the source: (a) CT images and (b) MR images. Rest of all the columns show the fused image produced by the (c) Method 1, (d) Method 2, (e) Method 3, (f) Method 4, (g) Method 5, (h) Method 6, (i) Method 7, (j) Method 8, (k) Proposed method.

**Method 9:** The proposed CT and MR fusion method where the NSML-PCNN is used for high frequency decomposition and a fusion map is generated by computing the RE for low frequency NSST coefficients. To implement the proposed fusion method, similar parameters as method 7 are used.

#### 4.2.1. Experiment 1

For the comparative analysis of the fusion results produced by the aforementioned methods, nine different pairs of the CT and MR brain images as shown in Fig. 4(a) and (b), respectively, are used. Their corresponding fused images are also shown in Fig. 4(c)–(k). From the visual analysis of all these results, it is observed that the proposed method is able to successfully preserve both the feature information such as bony structure of the CT images and soft tissue information of the MR image with better resolution as compared to other methods. For better presentation that also helps for visual analysis, the CT and MR image pair 4 and 8 are shown in Figs. 5 and 6, respectively. From these results mentioned in Figs. 5 and 6, it can be easily observed that the fused images provided by the proposed method are better than others.

Further, these subjective evaluations of the proposed and other methods are also supported by the quantitative results using six different performance measures as mentioned above. These objective outcomes obtained for different datasets using different fusion schemes are listed in Tables 1–6. From the results of the entropy mentioned in Table 1, it is seen that the proposed fusion method

gains higher entropy than the input CT and MR images and other methods. Sometimes, the WT based method 1 also achieves higher entropy values than others, but still it is less than the proposed method. Table 2 shows the standard deviation values of the source CT, MR and fused images produced by the different fusion methods. The higher value of the standard deviation of fused images reveals better contrast than the input images and other fused images produced by the other methods. Table 3 also shows the highest value of the MI that indicates the large amount of the information from the input CT and MR images is retained in the fused image generated by the proposed fusion method. Table 4 shows the spatial frequency as another performance metric value for the input and fused images obtained by the different fusion techniques. The higher SF values for the proposed method shows that the fused images obtained by the proposed fusion method have more information present in the source CT and MR images and also presents more activity and clarity level than the given input images. Besides it, the maximum value of the IQI shown in Table 5 ensures better quality of the fused images produced by the proposed fusion method as compared to others. Moreover, another parameter  $Q^{XY/F}$  is also evaluated for the entire test CT and MR images processed by all fusion method as mentioned above and listed in Table 6. From the results presented in Table 6, the higher value of  $Q^{XY/F}$  of the proposed method than others signifies that the proposed method is also able to preserve the edge information of the original CT and MR images in the fused images. Moreover, Table 7 provides a comparison of the averaged performance measure (mean  $\pm$  standard deviation) obtained by the

**Table 1**

Entropy values obtained by the different fusion schemes applied on the CT and MR images illustrated in Fig. 4.

Dataset	Source images		Fusion methods								
	CT	MR	Method 1	Method 2	Method 3	Method 4	Method 5	Method 6	Method 7	Method 8	Method 9
# 1	2.4224	4.4192	5.2127	5.0814	5.2057	5.1121	5.2727	5.2989	5.3401	5.2839	5.3430
# 2	3.0911	4.0592	4.8940	4.8612	4.8638	4.9348	4.9361	4.9914	4.9941	4.9362	5.0335
# 3	3.0809	3.5665	4.4542	4.5273	4.6208	4.6876	4.6935	4.7247	4.7301	4.7231	4.8078
# 4	3.3004	4.2197	5.2507	5.2802	5.2286	5.2871	5.3184	5.3486	5.3937	5.3255	5.4243
# 5	3.1549	4.0256	4.8650	4.7992	4.8337	4.8924	4.9108	4.9528	4.9768	4.9413	4.9927
# 6	3.1296	3.4987	4.1145	4.2413	4.2791	4.2841	4.3675	4.4379	4.5661	4.4298	4.6794
# 7	3.0159	3.4675	4.0108	4.0834	4.1262	4.1826	4.1897	4.5431	4.6669	4.2629	4.7696
# 8	2.8617	3.7134	4.7939	4.8264	4.8554	4.8586	4.8604	4.8970	4.9093	4.8878	4.9426
# 9	3.5252	3.9525	4.5105	4.6513	4.6864	4.6937	4.7240	4.7826	4.7990	4.7392	4.9018

**Table 2**

Standard deviation obtained by the different fusion schemes applied on the CT and MR images illustrated in Fig. 4.

Dataset	Source images		Fusion methods								
	CT	MR	Method 1	Method 2	Method 3	Method 4	Method 5	Method 6	Method 7	Method 8	Method 9
# 1	86.539	56.363	65.380	63.982	67.512	86.128	86.275	86.695	86.841	86.546	87.186
# 2	79.854	53.881	59.750	57.758	61.896	81.305	81.587	81.737	81.954	81.544	82.035
# 3	92.692	53.941	66.890	65.842	68.378	91.637	91.667	92.174	92.394	92.162	92.686
# 4	81.822	56.840	57.008	60.982	63.388	83.266	83.368	83.492	83.721	83.393	83.814
# 5	84.708	63.885	65.749	63.765	67.744	89.121	89.489	89.653	89.898	89.643	89.908
# 6	75.909	65.658	62.414	60.548	63.579	85.309	85.631	85.948	86.106	85.642	86.153
# 7	91.009	65.351	69.762	69.192	71.432	95.027	95.402	95.789	95.793	95.421	96.160
# 8	83.349	55.384	62.674	60.946	65.385	84.304	84.363	84.659	84.675	84.631	85.033
# 9	79.285	62.851	61.429	59.674	62.947	83.952	84.361	84.433	84.780	84.394	84.852

**Table 3**

Mutual information obtained by the different fusion schemes applied on the CT and MR images illustrated in Fig. 4.

Dataset	Fusion methods								
	Method 1	Method 2	Method 3	Method 4	Method 5	Method 6	Method 7	Method 8	Method 9
# 1	2.5634	3.0854	3.2190	3.1058	3.1384	3.2226	3.2462	3.1822	3.2956
# 2	2.5240	2.7632	2.9961	3.0139	3.0489	3.0644	3.0792	3.0604	3.0853
# 3	2.3354	2.4483	2.6345	2.9970	3.0389	3.0310	3.0594	3.0454	3.0724
# 4	2.1770	2.4156	2.7054	2.7727	2.8223	2.8432	2.8469	2.8377	2.8509
# 5	2.3399	2.5264	2.7793	2.9413	2.9532	2.9722	2.9865	2.9641	2.9886
# 6	2.6323	2.7924	3.1108	3.1173	3.1358	3.1570	3.1730	3.1544	3.2026
# 7	2.4357	2.5998	2.8338	3.0357	3.0390	3.0913	3.0978	3.0902	3.1514
# 8	2.3288	2.5726	2.8409	2.8499	2.8607	2.8813	2.8877	2.8624	2.8933
# 9	2.4310	2.6263	2.8091	3.0268	3.0406	3.0502	3.0569	3.0475	3.0973

**Table 4**

Spatial frequency obtained by the different fusion schemes applied on the CT and MR images illustrated in Fig. 4.

Dataset	Source images		Fusion methods								
	CT	MR	Method 1	Method 2	Method 3	Method 4	Method 5	Method 6	Method 7	Method 8	Method 9
# 1	4.5614	5.4908	5.1216	4.8845	5.2468	5.3696	5.4210	5.5828	5.6992	5.5582	5.7153
# 2	4.8211	6.4724	6.6219	6.2814	6.5585	6.3475	6.6242	6.6959	6.8099	6.3185	6.8577
# 3	5.2935	6.0960	5.5161	5.6126	6.0983	5.6933	5.8879	6.1315	6.1480	5.8938	6.2712
# 4	6.4645	8.1102	7.1815	7.1322	7.5095	7.2480	7.3292	7.6077	7.6801	7.4228	8.8396
# 5	5.4280	7.1188	6.5576	6.2480	6.7447	6.3264	6.6292	6.8515	6.9478	6.6472	7.7340
# 6	4.4296	5.3060	5.5684	5.3986	5.5623	5.4073	5.5829	5.7063	5.7910	5.6298	5.8769
# 7	4.8626	5.9404	6.3112	5.8942	5.9743	6.0055	6.2845	6.3453	6.3712	6.2919	6.4666
# 8	5.5095	6.1565	5.8714	6.0644	6.1661	6.1553	6.2186	6.4386	6.5236	6.3458	6.5816
# 9	6.0419	6.2869	6.0779	6.2712	6.5367	6.5796	6.7005	6.8568	6.8796	6.7025	6.9213

**Table 5**

IQI obtained by the different fusion schemes applied on the CT and MR images illustrated in Fig. 4.

Dataset	Fusion methods								
	Method 1	Method 2	Method 3	Method 4	Method 5	Method 6	Method 7	Method 8	Method 9
# 1	0.2822	0.3642	0.4204	0.4415	0.4542	0.4709	0.4764	0.4616	0.4839
# 2	0.3052	0.3311	0.4097	0.4128	0.4346	0.4482	0.4526	0.4401	0.4627
# 3	0.3290	0.3347	0.3997	0.4173	0.4354	0.4396	0.4490	0.4387	0.4833
# 4	0.3244	0.3945	0.4502	0.4278	0.4365	0.4553	0.4597	0.4423	0.4649
# 5	0.2964	0.3683	0.4336	0.4225	0.4303	0.4470	0.4583	0.4388	0.4602
# 6	0.2883	0.3404	0.4872	0.5131	0.5304	0.5482	0.5495	0.5422	0.5592
# 7	0.3655	0.3498	0.5218	0.5681	0.5702	0.5756	0.5825	0.5746	0.5857
# 8	0.3781	0.3702	0.4452	0.4662	0.4722	0.5023	0.5058	0.4855	0.5153
# 9	0.2856	0.3008	0.4295	0.4333	0.4477	0.4518	0.4527	0.4511	0.4557

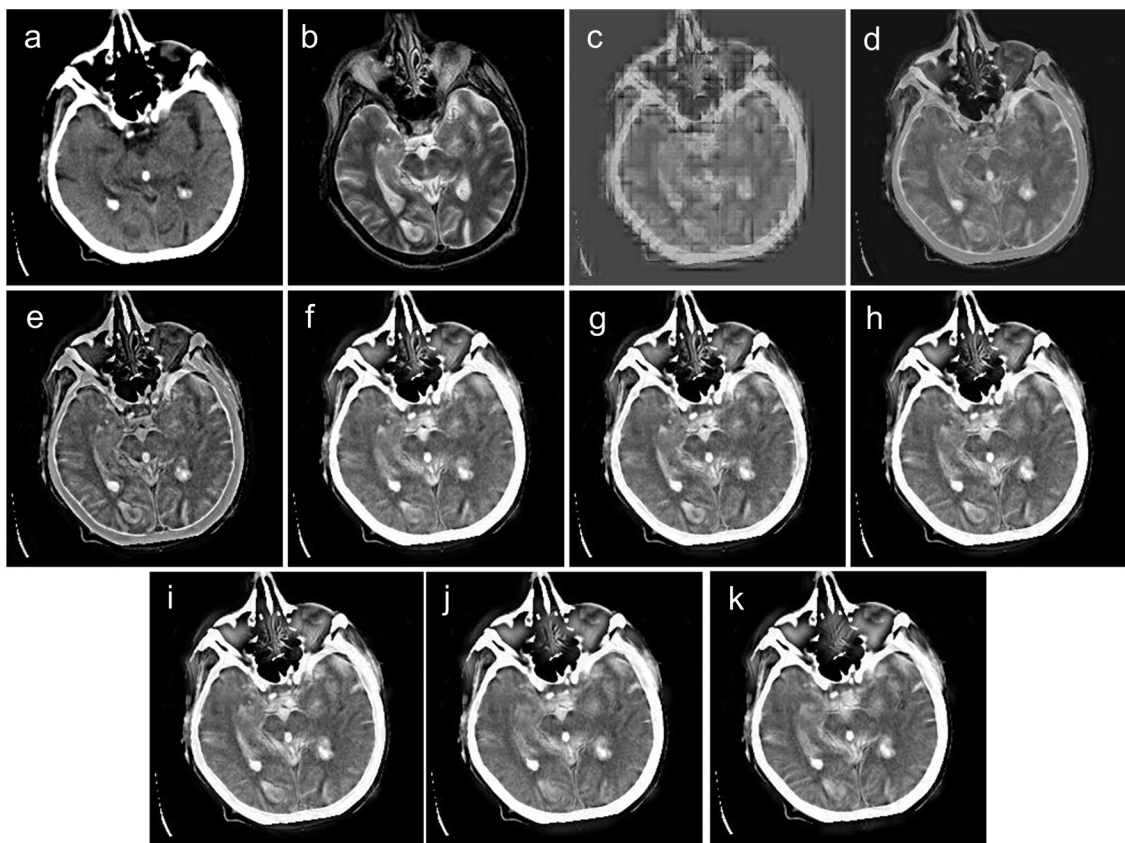


**Fig. 5.** Comparative analysis of visual results obtained by different fusion methods applied to the image pair-4: (a) CT image and (b) MR image. The fused image provided by the (c) Method 1, (d) Method 2, (e) Method 3, (f) Method 4, (g) Method 5, (h) Method 6, (i) Method 7, (j) Method 8, (k) Proposed method.

**Table 6**

Edge index ( $Q^{XY/F}$ ) obtained by the different fusion schemes applied on the CT and MR images illustrated in Fig. 4.

Dataset	Fusion methods								
	Method 1	Method 2	Method 3	Method 4	Method 5	Method 6	Method 7	Method 8	Method 9
# 1	0.2769	0.3847	0.4380	0.4299	0.4375	0.4494	0.4631	0.4480	0.4685
# 2	0.2586	0.3624	0.4592	0.4636	0.5088	0.5134	0.5164	0.5098	0.5496
# 3	0.2592	0.3516	0.4059	0.4172	0.4234	0.4261	0.4347	0.4236	0.5002
# 4	0.2502	0.3592	0.4963	0.4692	0.4866	0.5122	0.5143	0.4962	0.5255
# 5	0.2405	0.3478	0.4847	0.4723	0.4729	0.4919	0.4964	0.4843	0.5188
# 6	0.2669	0.3514	0.4736	0.4957	0.4975	0.5112	0.5283	0.5008	0.5514
# 7	0.2758	0.4208	0.5163	0.4805	0.4825	0.5231	0.5399	0.5211	0.5970
# 8	0.2929	0.4116	0.5448	0.5490	0.5772	0.5797	0.5856	0.5784	0.5930
# 9	0.2395	0.3358	0.4102	0.4164	0.4203	0.4244	0.4295	0.4211	0.4969

**Table 7**

Comparative analysis of the averaged performance measures obtained by the proposed method and others for dataset-1.

Methods	EN	MI	STD	SF	IQI	$Q^{XY/F}$
Source CT	$3.0647 \pm 0.3035$	–	$83.9079 \pm 5.4953$	$5.2680 \pm 0.6784$	–	–
Source MR	$3.8803 \pm 0.3366$	–	$59.3509 \pm 4.9843$	$6.3309 \pm 0.8517$	–	–
Method 1	$4.6785 \pm 0.4401$	$2.4186 \pm 0.1404$	$63.4506 \pm 3.8991$	$6.0920 \pm 0.6451$	$0.3172 \pm 0.0351$	$0.2623 \pm 0.0177$
Method 2	$4.7057 \pm 0.3802$	$2.6478 \pm 0.2069$	$62.5210 \pm 3.5133$	$5.9763 \pm 0.6386$	$0.3504 \pm 0.0274$	$0.3694 \pm 0.0297$
Method 3	$4.7444 \pm 0.3707$	$2.8810 \pm 0.1908$	$65.8068 \pm 3.1501$	$6.2664 \pm 0.6702$	$0.4441 \pm 0.0387$	$0.4699 \pm 0.0468$
Method 4	$4.7703 \pm 0.3585$	$2.9845 \pm 0.1133$	$86.6721 \pm 4.4163$	$6.1258 \pm 0.5964$	$0.4558 \pm 0.0524$	$0.4660 \pm 0.0421$
Method 5	$4.8081 \pm 0.3713$	$3.0086 \pm 0.1102$	$86.9047 \pm 4.4341$	$6.2976 \pm 0.6017$	$0.4679 \pm 0.0494$	$0.4785 \pm 0.0490$
Method 6	$4.8863 \pm 0.3073$	$3.0348 \pm 0.1218$	$87.1756 \pm 4.5285$	$6.4685 \pm 0.6267$	$0.4821 \pm 0.0493$	$0.4924 \pm 0.0508$
Method 7	$4.9307 \pm 0.2848$	$3.0482 \pm 0.1267$	$87.3512 \pm 4.4871$	$6.5389 \pm 0.6230$	$0.4874 \pm 0.0486$	$0.5009 \pm 0.0510$
Method 8	$4.8366 \pm 0.3499$	$3.0271 \pm 0.1189$	$87.0419 \pm 4.4968$	$6.3123 \pm 0.5819$	$0.4750 \pm 0.0503$	$0.4870 \pm 0.0503$
Proposed method	$4.9883 \pm 0.2508$	$3.0708 \pm 0.1423$	$87.5363 \pm 4.5573$	$6.8071 \pm 0.9693$	$0.4968 \pm 0.0470$	$0.5334 \pm 0.0435$

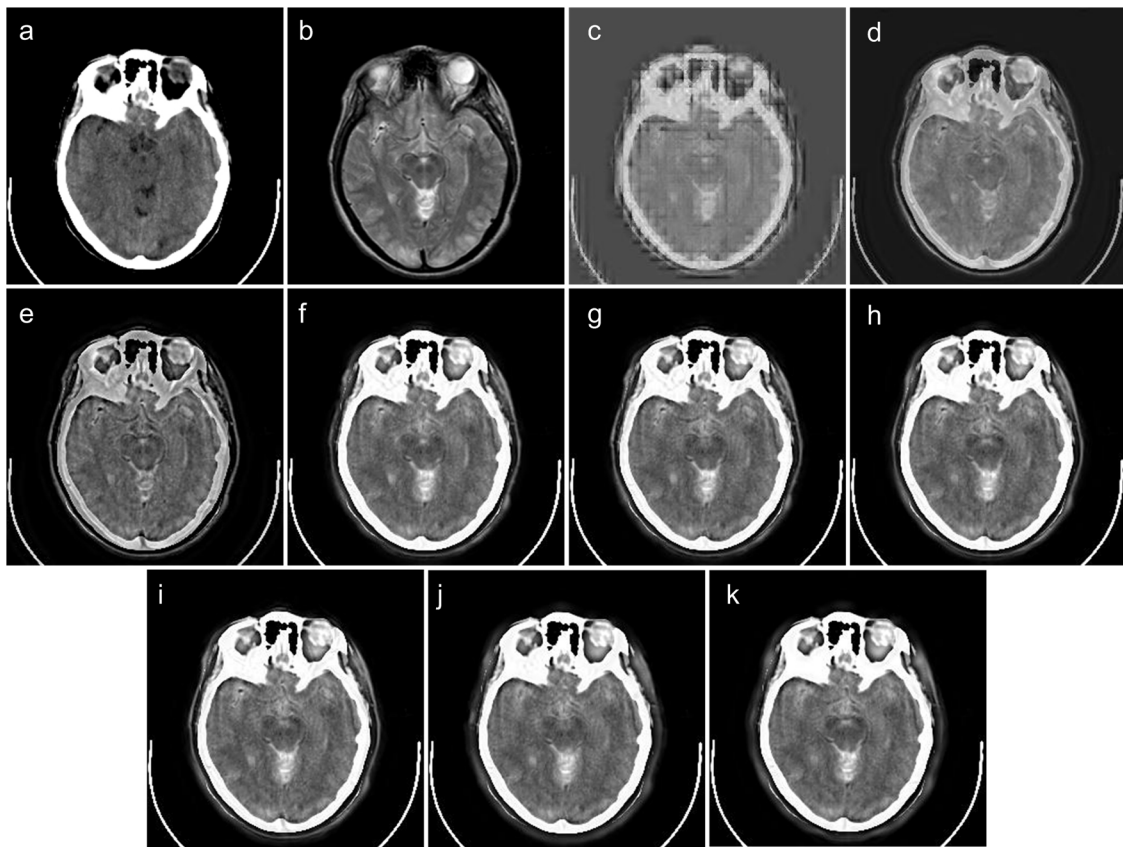


**Fig. 6.** Comparative analysis of visual results obtained by different fusion methods applied to the eight image pair-8: (a) CT image and (b) MR image. The fused image provided by the (c) Method 1, (d) Method 2, (e) Method 3, (f) Method 4, (g) Method 5, (h) Method 6, (i) Method 7, (j) Method 8, (k) Proposed method.

aforementioned fusion methods. Furthermore, from the objective analysis of all the results mentioned in Tables 1–7, it can be summarized that

- The NSST based fusion method obviously outperforms the other fusion methods. The proposed fusion scheme achieves 62.76%, 28.56% higher entropy than source CT and MR images, respectively. Moreover, the proposed method gains approx 6.62%, 6.07%, 5.1%, 4.56%, 3.74%, 2.08%, 1.16% and 3.14% higher entropy than the methods 1–8, respectively. These results ensure that the more information lies in the fused images obtained by the produced method than others.
- The proposed method also reveals an improvement in the contrast resolution of the fused images as compared to others by achieving the 37.95%, 41.09%, 33.02%, 0.57–0.997% and 0.21–0.41% larger standard deviation of the fused images than WT\_AVG\_MAX, NSCT\_AVG\_MAX, NSST\_AVG\_MAX, NSCT\_PCNN based methods and NSST\_PCNN based methods, respectively. Generally, the CT images have better contrast than the MR images with high standard deviation values and the proposed method also gains the better STD values than both the CT and MR images.
- The larger value of the MI and SF metric of the fused images produced by the proposed method assures the more information preservation and more activity and clarity level in the fused images. It gains approx 11.73%, 7–11% and 4–5% higher SF values than the WT, NSCT and NSST based fusion method, respectively. Moreover, it has 26.9% and 1.44–26.21% larger MI values than the WT and NSCT based fusion method, respectively.
- Finally, the proposed method also gets higher values of both the quality and edge index that provide better quality of the fused images with more edge preservation. The averaged IQI

values obtained by the proposed method increase by approximately 4–8% and 1–3% from the NSCT and NSST based PCNN models. Moreover, the proposed method achieves approximately 9.5–14.5% and 8.5% larger  $Q^{XY/F}$  values than the NSCT and NSST based fusion algorithms, respectively.

Hence, on the basis of quantitative and visual analysis of results, it is observed that the proposed fusion algorithm outperforms the others by producing good quality of fused images with more details and edge information present in the source

**Table 8**  
Comparative performance of the proposed method with others for the image dataset illustrated in Fig. 7.

Fusion schemes	MI	EN	STD
Scheme [38]	2.368	–	–
Scheme [38]	5.093	5.911	–
Scheme [38]	2.410	–	–
Scheme [24,45]	2.057	4.982	33.65
Scheme [24,46]	2.714	6.729	57.97
Scheme [24,47]	2.529	6.387	53.82
Scheme [48]	–	5.990	32.90
Scheme [7,44]	3.073	6.096	41.56
Scheme [44]	2.748	6.199	40.56
Scheme [11]	3.318	6.065	40.22
Scheme [49]	–	6.730	60.32
Scheme [24,35]	3.734	6.771	59.83
Scheme [24]	3.452	6.767	59.85
Scheme [47]	–	6.387	53.82
NSST_MAX_SF_PCNN [37]	3.793	6.780	60.02
NSST_MAX_NMSF_PCNN	4.100	6.801	60.11
NSCT.RE_NSML_PCNN	3.774	6.777	62.03
Proposed method	4.155	6.835	62.17

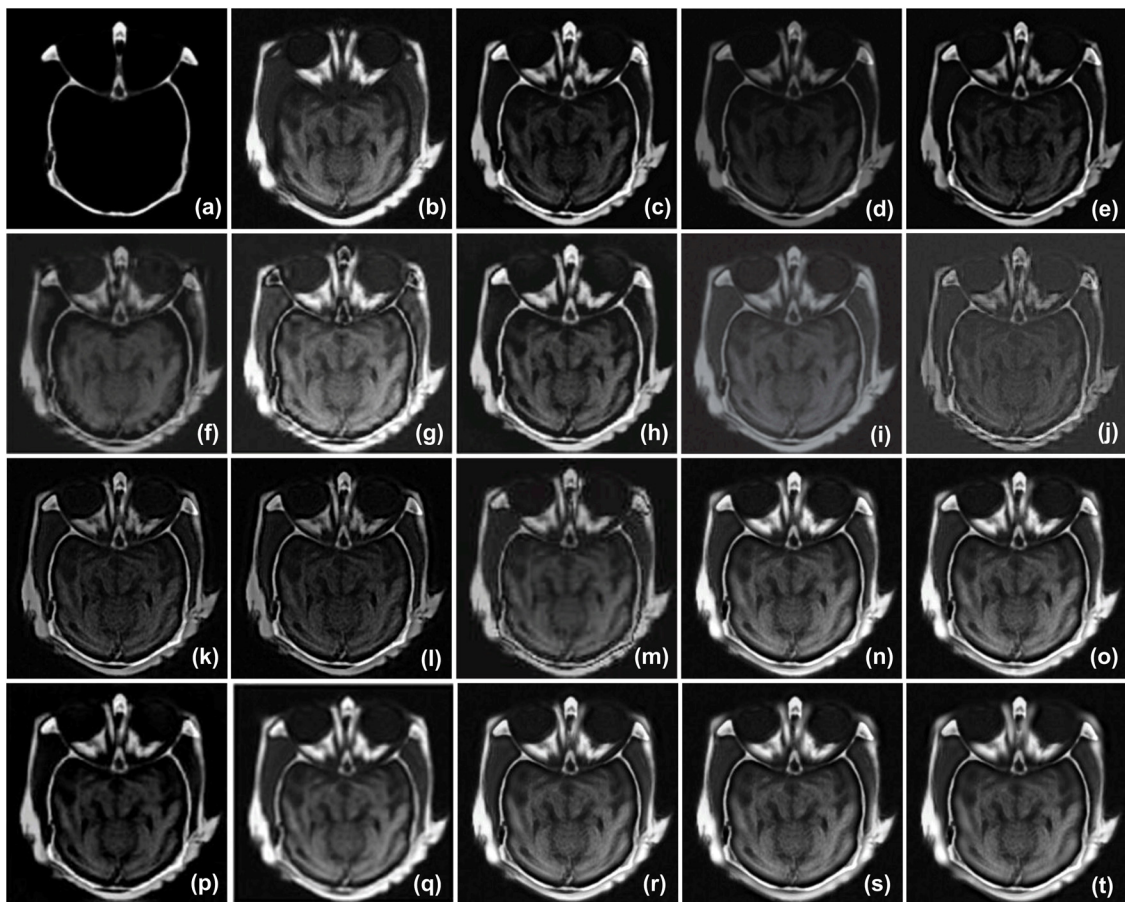


**Fig. 7.** Comparative performance of the different fusion methods applied to another dataset. (a) CT image, (b) MR image, (c) Scheme [38], (d) Scheme [38], (e) Scheme [38], (f) Scheme [24,45], (g) Scheme [24,46], (h) Scheme [24,47], (i) Scheme [48], (j) Scheme [7,44], (k) Scheme [44], (l) Scheme [11], (m) Scheme [49], (n) Scheme [24,35], (o) Scheme [24], (p) Scheme [47], (q) NSST\_MAX\_SF\_PCNN [37], (r) NSST\_MAX\_MSF\_PCNN method, (s) NSCT\_RE\_NSML\_PCNN method (t) Proposed method.

images. Moreover, one important analysis of time taken by each fusion scheme, individually is also done. As mentioned above, the time cost of the NSST is lower than the NSCT. Therefore, the NSCT\_AVG\_MAX takes too much time in comparison to the NSST\_AVG\_MAX, but the NSST\_MAX\_SF\_PCNN has the higher time cost than the NSCT\_AVG\_MAX due to additional PCNN analysis in the fusion process. Similarly, the time taken by the fusion methods such as NSCT\_MAX\_SF\_PCNN and NSCT.RE\_NSML\_PCNN is higher than the NSST\_MAX\_SF\_PCNN and NSST.RE\_NSML\_PCNN methods, respectively because of the higher time cost of the NSCT.

#### 4.2.2. Experiment 2

To further investigate the performance of the proposed method with others, various fusion methods presented in the literature are considered and the second datasets are processed by all these fusion methods. Their corresponding fused images are shown in Fig. 7. As per the discussion with an expert about the visual analysis of the experimental results shown in Fig. 7, the proposed fusion scheme provides better results compared to others. Besides the visual analysis of the image, the experimental results are also mentioned in Table 8. These results also show that the proposed method gains larger MI values than the others except for the pixel averaging based fusion schemes as this method is applied to the image intensity values in spatial domain. It also achieves higher EN values than other methods. Moreover, the fused images obtained by the proposed method have better contrast by obtaining higher STD values as compared to other existing methods.

## 5. Conclusions

In this paper, a new fusion method for the CT and MR medical images is presented that is based on the NSML motivated PCNN as a bio inspired neural network in the NSST domain. In the proposed method, the NSST provides both the multiscale and direction analysis of the original image. The regional energy based an activity level measure is used for fusing the low frequency subband coefficients. Experiments were carried out on the different pairs of CT and MR images to make subjective evaluations. The proposed fusion scheme is also compared with the various fusion rules based on the different transformation techniques, such as the WT, NSCT and NSST. Moreover, the results obtained by the proposed method are also compared with the PCNN based fusion scheme in different domain. From the experimental results, it is observed that the proposed fusion algorithm outperforms others not only in terms of visual analysis, but also in terms of different performance measures by preserving the soft tissue structure from the MR images and bony structure from the CT images.

## References

- [1] C. Pohl, J.L. Van Genderen, Multisensor image fusion in remote sensing: concepts, methods and applications, *Int. J. Remote Sens.* 19 (1998) 823–854.
- [2] H. Ghassemian, A retina based multi-resolution image-fusion, in: Proceedings of the International Symposium on Geoscience and Remote Sensing, vol. 702, 2001, pp. 709–711.
- [3] K. Baum, M. Helguera, A. Krol, Fusion viewer: a new tool for fusion and visualization of multimodal medical data sets, *J. Digit. Imaging* 21 (2008) 59–68.

- [4] G. Piella, H. Heijmans, A new quality metric for image fusion, in: Proceedings of the IEEE International Conference on Image Processing, 2003, pp. III-173–III-176.
- [5] P.J. Burt, E.H. Adelson, The Laplacian pyramid as a compact image code, *IEEE Trans. Commun.* 31 (1983) 532–540.
- [6] A. Toet, Image fusion by a ratio of low-pass pyramid, *Pattern Recogn. Lett.* 9 (4) (1989) 245–253.
- [7] H. Li, B.S. Manjunath, S.K. Mitra, Multisensor image fusion using the wavelet transform, *J. Graph. Model Image Process.* 57 (1995) 235–245.
- [8] K. Amolins, Y. Zhang, P. Dare, Wavelet based image fusion techniques – an introduction, review and comparison, *ISPRS J. Photogramm. Remote Sens.* 62 (2007) 249–263.
- [9] M.N. Do, M. Vetterli, The finite ridgelet transform for image representation, *IEEE Trans. Image Process.* 12 (2003) 16–28.
- [10] J.L. Starck, E.J. Candès, D.L. Donoho, The curvelet transform for image denoising, *IEEE Trans. Image Process.* 11 (2002) 670–684.
- [11] Q.-G. Miao, C. Shi, P.-F. Xu, M. Yang, Y.-B. Shi, A novel algorithm of image fusion using shearlets, *Opt. Commun.* 284 (2011) 1540–1547.
- [12] M.N. Do, M. Vetterli, The contourlet transform: an efficient directional multiresolution image representation, *IEEE Trans. Image Process.* 14 (2005) 2091–2106.
- [13] Q. Miao, B. Wang, The contourlet transform for image fusion, in: Proceedings of the Defense and Security Symposium, 2006, pp. 62420–62428.
- [14] W. Kong, Y. Lei, Technique for image fusion between gray-scale visual light and infrared images based on NSST and improved RF, *Optik* 124 (2013) 6423–6431.
- [15] A.L. da Cunha, Z. Jianping, M.N. Do, The nonsubsampled contourlet transform: theory, design, and applications, *IEEE Trans. Image Process.* 15 (2006) 3089–3101.
- [16] D. Labate, W.-Q. Lim, G. Kutyniok, G. Weiss, Sparse multidimensional representation using shearlets, in: Proceedings of the SPIE, 2005, pp. 254–262.
- [17] G. Easley, D. Labate, W.-Q. Lim, Sparse directional image representations using the discrete shearlet transform, *Appl. Comput. Harm. Anal.* 25 (2008) 25–46.
- [18] C. Yuan, L. Shutao, H. Jianwen, Multi-focus image fusion by nonsubsampled shearlet transform, in: Proceedings of the Sixth International Conference on Image and Graphics, 2011, pp. 17–21.
- [19] W. Kong, J. Liu, Technique for image fusion based on NSST domain improved fast non-classical RF, *Infrared Phys. Technol.* 61 (2013) 27–36.
- [20] B. Yang, S. Li, F. Sun, Image fusion using nonsubsampled contourlet transform, in: Proceedings of the IEEE Fourth International Conference on Image and Graphics, 2007, pp. 719–724.
- [21] R. Balasubramanian, G. Bhatnagar, A new contrast based image fusion using wavelet packets, in: Proceedings of the IEEE Conference on Applications of Intelligent Systems, 2008, pp. 141–145.
- [22] S. Li, B. Yang, Multifocus image fusion by combining curvelet and wavelet transform, *Pattern Recogn. Lett.* 29 (2008) 1295–1301.
- [23] P. Ganapala, V. Kumar, CT and MR image fusion scheme in nonsubsampled contourlet transform domain, *J. Digit. Imaging* 27 (2014) 407–418.
- [24] S. Das, M. Kundu, NSCT-based multimodal medical image fusion using pulse-coupled neural network and modified spatial frequency, *Med. Biol. Eng. Comput.* 50 (2012) 1105–1114.
- [25] H. Li, Y. Chai, Z. Li, Multi-focus image fusion based on nonsubsampled contourlet transform and focused regions detection, *Optik* 124 (2013) 40–51.
- [26] L. Wang, B. Li, L.-f. Tian, Multi-modal medical image fusion using the inter-scale and intra-scale dependencies between image shift-invariant shearlet coefficients, *Inf. Fusion* 19 (2014) 20–28.
- [27] W. Kong, Technique for gray-scale visual light and infrared image fusion based on non-subsampled shearlet transform, *Infrared Phys. Technol.* 63 (2014) 110–118.
- [28] H.S. Ranganath, G. Kuntimad, J.L. Johnson, Pulse coupled neural networks for image processing, in: Proceedings of the IEEE Visualize the Future, 1995, pp. 37–43.
- [29] Z. Wang, Y. Ma, F. Cheng, L. Yang, Review of pulse-coupled neural networks, *Image Vis. Comput.* 28 (2010) 5–13.
- [30] P. Geng, X. Zheng, Z. Zhang, Y. Shi, S. Yan, Multifocus image fusion with PCNN in shearlet domain, *Res. J. Appl. Sci. Eng. Technol.* 4 (2012) 2283–2290.
- [31] J.M. Kinser, Pulse-coupled image fusion, *Opt. Eng.* 36 (1997) 737–742.
- [32] W. Li, X.-F. Zhu, A new algorithm of multi-modality medical image fusion based on pulse-coupled neural networks, in: Advances in Natural Computation, Springer, 2005, pp. 995–1001.
- [33] W. Li, X.-F. Zhu, A new image fusion algorithm based on wavelet packet analysis and PCNN, in: Proceedings of the IEEE International Conference on Machine Learning and Cybernetics, 2005, pp. 5297–5301.
- [34] W. Huang, Z. Jing, Multi-focus image fusion using pulse coupled neural network, *Pattern Recogn. Lett.* 28 (2007) 1123–1132.
- [35] X.-B. Qu, J.-W. Yan, H.-Z. Xiao, Z.-Q. Zhu, Image fusion algorithm based on spatial frequency-motivated pulse coupled neural networks in non-subsampled contourlet transform domain, *Acta Automat. Sin.* 34 (2008) 1508–1514.
- [36] L. Fu, L. Yifan, L. Xin, Image fusion based on nonsubsampled contourlet transform and pulse coupled neural networks, in: Proceedings of the IEEE International Conference on Intelligent Computation Technology and Automation, 2011, pp. 572–575.
- [37] P. Geng, Z. Wang, Z. Zhang, Z. Xiao, Image fusion by pulse couple neural network with shearlet, *Opt. Eng.* 51 (2012) 067005.
- [38] Z. Wang, Y. Ma, Medical image fusion using m-PCNN, *Inf. Fusion* 9 (2008) 176–185.
- [39] M.M. Deepika, V. Vaithyanathan, An efficient method to improve the spatial property of medical images, *J. Theor. Appl. Inf. Technol.* 35 (2012) 141–148.
- [40] Y. Chai, H. Li, X. Zhang, Multifocus image fusion based on features contrast of multiscale products in nonsubsampled contourlet transform domain, *Optik* 123 (2012) 569–581.
- [41] S. Yang, M. Wang, Y. Lu, W. Qi, L. Jiao, Fusion of multiparametric SAR images based on SW-nonsubsampled contourlet and PCNN, *Signal Process.* 89 (2009) 2596–2608.
- [42] Z. Wang, A.C. Bovik, A universal image quality index, *IEEE Signal Process. Lett.* 9 (2002) 81–84.
- [43] C.S. Xydeas, V. Petrovic, Objective image fusion performance measure, *Electron. Lett.* 36 (2000) 308–309.
- [44] S. Li, B. Yang, J. Hu, Performance comparison of different multi-resolution transforms for image fusion, *Inf. Fusion* 12 (2011) 74–84.
- [45] T. Hua, F. Ya-Nan, W. Pei-Guang, Image fusion algorithm based on regional variance and multi-wavelet bases, in: Proceedings of the International Conference on Future Computer and Communication, 2010, pp. 792–795.
- [46] Y. Yang, D.S. Park, S. Huang, N. Rao, Medical image fusion via an effective wavelet-based approach, *EURASIP J. Adv. Signal Process.* 2010 (2010) 1–13.
- [47] L. Yang, B. Guo, W. Ni, Multimodality medical image fusion based on multi-scale geometric analysis of contourlet transform, *Neurocomputing* 72 (2008) 203–211.
- [48] R. Singh, A. Khare, Fusion of multimodal medical images using Daubechies complex wavelet transform – a multiresolution approach, *Inf. Fusion* 19 (2014) 49–60.
- [49] C. Kavitha, C. Chellamuthu, R. Rajesh, Medical image fusion using combined discrete wavelet and ripplet transforms, *Proc. Eng.* 38 (2012) 813–820.